3-2019

Shaping the Far-zone Intensity, Degree of Polarization, Angle of Polarization, and Ellipticity Angle Using Vector Schell-model Sources

Milo W. Hyde IV
Air Force Institute of Technology

Recommended Citation

Hyde, M. W. (2019). Shaping the far-zone intensity, degree of polarization, angle of polarization, and ellipticity angle using vector Schell-model sources. Results in Physics, 12, 2242–2250. https://doi.org/10.1016/j.rinp.2019.02.008

Results in Physics 12 (2019) 2242–2250

Contents lists available at ScienceDirect

Results in Physics

journal homepage: www.elsevier.com/locate/rinp

Shaping the far-zone intensity, degree of polarization, angle of polarization, and ellipticity angle using vector Schell-model sources

Milo W. Hyde IV[1]

Department of Electrical and Computer Engineering, Air Force Institute of Technology, Dayton, OH 45433, USA

ARTICLE INFO

Keywords:
Beam shaping
Coherence
Polarization
Random sources
Schell-model sources
Statistical optics

ABSTRACT

This paper presents a method to control both the shape and polarization of a beam in the far field using a vector Schell-model source. Given a desired far-zone beam shape and polarization, and applying Fourier and statistical optics theory, we derive the requisite second-order moments of said source, discuss what aspects of the far-zone beam can be controlled, and develop a step-by-step procedure for synthesizing the required random vector field instances. We validate this approach with Monte-Carlo wave-optics simulations. The results are found to be in very good agreement with the desired far-zone beam characteristics. The beam-shaping technique developed in this paper will find use in optical trapping, optical communications, directed energy, remote sensing, and medical applications.

Introduction

Designing light's shape, polarization, and coherence has numerous applications including optical trapping, optical communications, directed energy, remote sensing, and medicine [1–5]. For this reason, the literature is replete with scalar and vector sources, with partial spatial coherence, that have interesting and complex behaviors, e.g., beams that self focus, self steer, self split, rotate, et cetera [6–13].

Physically realizing, or synthesizing, these sources is also a very active area of research. The most common approach is to use one or more spatial light modulators in an interferometer-like set-up to generate vector field instances [1–4,14–21]. The plethora of vector beams that can be synthesized using this technique is quite extraordinary [2,3,14–16,19–23].

The primary objective of these efforts has been to generate the desired source, i.e., control the field's shape, polarization, or coherence, in the source plane. Few studies have dealt with controlling these parameters at another axial location—at the focus of a lens, for instance. This ability is crucial for all the applications listed above. Of the studies that focused on controlling beam parameters at the focus of a lens (or equivalently, in the far zone of the source), all have dealt with scalar partially coherent sources and only controlled beam shape [24–27].

In this paper, we extend the prior scalar work to control both beam shape and polarization in the far zone of the source. Using Fourier and statistical optics theory, we first derive expressions for the spatial correlation functions (or via Fourier transforms, the spatial power spectra) of a vector Schell-model source that radiates a beam with desired, or designed, far-zone shape and polarization properties. We discuss what aspects of the resulting beam can be controlled, and develop a procedure (or recipe) to synthesize the required vector field instances.

Next, we validate the analysis and synthesis procedure with Monte-Carlo wave-optics simulations. As a proof of concept, we synthesize vector Schell-model sources that radiate far-zone beams with shapes and polarization parameters that are complex grayscale images. We quantitatively assess the results by computing the correlation coefficients versus trial number to study the convergence of the random vector field instances to the desired shape and polarization images.

Lastly, we conclude with a summary of the work presented in the paper and a brief list of potential applications.

Theory

Here, we present the underlying Fourier and statistical optics theory necessary to design a vector Schell-model source that radiates a far-zone beam with a desired shape and polarization properties. In the first half of this section, we discuss the theoretical assumptions, present a model for stochastic vector fields, derive the statistical far-zone

E-mail address: milo.hyde@us.af.mil.

[1] The views expressed in this paper are those of the authors and do not reflect the official policy or position of the U.S. Air Force, the Department of Defense, or the U.S. Government.

https://doi.org/10.1016/j.rinp.2019.02.008
Received 14 December 2018; Received in revised form 29 January 2019; Accepted 4 February 2019
Available online 08 February 2019

behavior of the random vector fields, and lastly, show how to generate vector field realizations with desired statistics. In the latter half of this section, we delve into the mathematical particulars of controlling the far-zone beam's shape and polarization. We derive expressions for the required statistics of the vector Schell-model source, and discuss what aspects of the beam can be controlled. We close this section with an enumerated procedure, which concisely summarizes the theory presented herein and provides a recipe for generating optical fields that, in the far field, result in a beam with desired complex shape and polarization characteristics.

Preliminaries

Assumptions

The goal here is to design a vector partially coherent source that produces a far-zone beam with desired shape (or intensity) and polarization properties. To this end, we make two assumptions that significantly simplify the analysis, while not overly restricting the applicability. The first is that the shapes of the field's x and y components (also called the component spectral densities, S_x and S_y, respectively) are equal in the source plane. This has the physical consequence that the polarization state across the source is uniform [4,28,29]. The second assumption is that the vector spatial correlation functions are much narrower (are fast functions) compared to the associated component spectral densities. This assumption is known in the literature as the quasi-homogeneous approximation, and the partially coherent source is referred to as a quasi-homogeneous electromagnetic source [4,30]. The cross-spectral density (CSD) matrix $\underline{\mathbf{W}}$ for such a source is

$$W_{ij}(\boldsymbol{\rho}_1, \boldsymbol{\rho}_2) = \left[S_i\left(\frac{\boldsymbol{\rho}_1 + \boldsymbol{\rho}_2}{2}\right) S_j\left(\frac{\boldsymbol{\rho}_1 + \boldsymbol{\rho}_2}{2}\right)\right]^{1/2} \mu_{ij}(\boldsymbol{\rho}_1 - \boldsymbol{\rho}_2), \tag{1}$$

where W_{ij} is the i^{th}, j^{th} element of $\underline{\mathbf{W}}$, S_i is the spectral density of the i^{th} field component, μ_{ij} is the cross-correlation function between the i^{th} and j^{th} field components, and $i, j = x, y$. The transverse position vectors $\boldsymbol{\rho}_1$ and $\boldsymbol{\rho}_2$ are $\boldsymbol{\rho}_{1,2} = \hat{\boldsymbol{x}} x_{1,2} + \hat{\boldsymbol{y}} y_{1,2}$.

Stochastic vector field

Let an instance of a random optical vector field be

$$\boldsymbol{E}(\boldsymbol{\rho}) = \hat{\boldsymbol{x}} C_x A(\boldsymbol{\rho}) T_x(\boldsymbol{\rho}) + \hat{\boldsymbol{y}} C_y A(\boldsymbol{\rho}) T_y(\boldsymbol{\rho}), \tag{2}$$

where C_i is the complex amplitude and T_i is the stochastic complex transmittance screen for the i^{th} component of the field, respectively. A is the amplitude function (beam shape) of the source; recall that $A_x = A_y = A$.

Taking the vector autocorrelation of (2) to form $\underline{\mathbf{W}}$ [4,28,29] produces

$$W_{ij}(\boldsymbol{\rho}_1, \boldsymbol{\rho}_2) = \langle E_i(\boldsymbol{\rho}_1) E_j^*(\boldsymbol{\rho}_2)\rangle = C_i C_j^* A(\boldsymbol{\rho}_1) A(\boldsymbol{\rho}_2) \langle T_i(\boldsymbol{\rho}_1) T_j^*(\boldsymbol{\rho}_2)\rangle, \tag{3}$$

where $\langle\rangle$ is the average taken over all complex screen realizations. By comparing this result to (1), it is clear that

$$\begin{aligned} S_i(\boldsymbol{\rho}) &= |C_i|^2 A^2(\boldsymbol{\rho}) \\ \mu_{ij}(\boldsymbol{\rho}_1 - \boldsymbol{\rho}_2) &= \langle T_i(\boldsymbol{\rho}_1) T_j^*(\boldsymbol{\rho}_2)\rangle. \end{aligned} \tag{4}$$

Note that $\arg(C_x C_y^*)$ is generally a free parameter and comes into play when dealing with circular polarization. We return to these expressions later in the paper.

Far-zone $\underline{\mathbf{W}}(\boldsymbol{\rho}, \boldsymbol{\rho})$

To control the intensity and polarization in the far zone, we require the far-zone, single-point $\underline{\mathbf{W}}$, i.e., $\underline{\mathbf{W}}$ evaluated at $\boldsymbol{\rho}_1 = \boldsymbol{\rho}_2 = \boldsymbol{\rho}$. This can be found by propagating the W_{ij} in (3) to the far field (a four-dimensional spatial Fourier transform [28,31]) and evaluating the resulting expression at $\boldsymbol{\rho}_1 = \boldsymbol{\rho}_2 = \boldsymbol{\rho}$. This expression takes the form

$$\begin{aligned} W_{ij}(\boldsymbol{\rho}, \boldsymbol{\rho}, z) = \frac{C_i C_j^*}{(\lambda z)^2} \iint \iint_{-\infty}^{\infty} A(\boldsymbol{\rho}_1') A(\boldsymbol{\rho}_2') \mu_{ij}(\boldsymbol{\rho}_1' - \boldsymbol{\rho}_2') \\ \times \exp\left[-\mathrm{j}\frac{k}{z}(\boldsymbol{\rho}_1' - \boldsymbol{\rho}_2')\cdot\boldsymbol{\rho}\right] \mathrm{d}^2\boldsymbol{\rho}_1' \, \mathrm{d}^2\boldsymbol{\rho}_2', \end{aligned} \tag{5}$$

where $k = 2\pi/\lambda$, λ is the wavelength, and z is the distance to the far-field observation plane. Making the variable transformations $\boldsymbol{s} = \boldsymbol{\rho}_1'$ and $\boldsymbol{t} = \boldsymbol{\rho}_1' - \boldsymbol{\rho}_2'$ simplifies (5) to

$$\begin{aligned} W_{ij}(\boldsymbol{\rho}, \boldsymbol{\rho}, z) = \frac{C_i C_j^*}{(\lambda z)^2} \iint_{-\infty}^{\infty} \mu_{ij}(\boldsymbol{t}) \exp\left(-\mathrm{j}\frac{k}{z}\boldsymbol{t}\cdot\boldsymbol{\rho}\right) \\ \times \iint_{-\infty}^{\infty} A(\boldsymbol{s}) A(\boldsymbol{s} - \boldsymbol{t}) \mathrm{d}^2 s \, \mathrm{d}^2 t. \end{aligned} \tag{6}$$

The amplitude function integrals are equal to the autocorrelation of A, represented hereafter as $\mathcal{A}(\boldsymbol{t})$. Recall that A was assumed to vary much more slowly (be much broader) than μ_{ij}—the source was assumed to be an electromagnetic quasi-homogeneous source. This means that $\mathcal{A}$ also varies much more slowly than μ_{ij}, such that

$$\begin{aligned} W_{ij}(\boldsymbol{\rho}, \boldsymbol{\rho}, z) &\approx \frac{C_i C_j^*}{(\lambda z)^2} \mathcal{A}(0) \iint_{-\infty}^{\infty} \mu_{ij}(\boldsymbol{t}) \exp\left(-\mathrm{j}\frac{k}{z}\boldsymbol{t}\cdot\boldsymbol{\rho}\right) \mathrm{d}^2 t \\ &= \frac{C_i C_j^*}{(\lambda z)^2} \mathcal{A}(0) \Phi_{ij}\left(\frac{\boldsymbol{\rho}}{\lambda z}\right), \end{aligned} \tag{7}$$

where Φ_{ij}, by the Wiener-Khinchin theorem [28,29,31], is the spatial cross-power spectrum of the i^{th} and j^{th} field components.

Eq. (7) is a specialization of the generalized van Cittert-Zernike theorem [28,31] and has been used in the past to generate a scalar Schell-model source which produces any desired shape in the far field [24–27]. Here, we use it to generate a vector Schell-model source that radiates a beam with a desired shape and polarization characteristics.

In contrast to the prior scalar work where any shape could be produced, here, the correlation functions of the x and y components of the field (μ_{xx} and μ_{yy}, respectively) ultimately determine the vector cross-correlation function μ_{xy}. This fundamentally limits what we can control. We discuss this in more detail in the following sections.

T_x, T_y, and μ_{xy}

To produce an instance of a vector source, given in (2), that radiates a beam with the far-zone, single-point W_{ij} given in (7), one must generate T_x and T_y with the proper statistics. The most common way of achieving this is to spatially filter two, two-dimensional arrays (one representing T_x, the other T_y) of circular complex, Gaussian random numbers [4,15,17,18,32–34]. The x and y spatial filters are related to the corresponding vector spatial correlation functions, namely, μ_{xx} and μ_{yy}. For computational efficiency, it is best to perform the filtering in the spectral domain using the convolution theorem.

To produce a source that radiates a beam in a general polarization state, $\mu_{xy} \neq 0$, which means that T_x and T_y must be generated from correlated Gaussian random numbers. To see how the statistics of T_x and T_y affect μ_{xy}, we note that a realization of discrete T_x (or T_y) can be produced by [15,24,26,32]

$$T_x[k, l] = \sum_m \sum_n r_x[m, n] \sqrt{\frac{\Phi_{xx}[m, n]}{2L_x L_y}} \exp\left(\mathrm{j}\frac{2\pi}{N_x} mk\right) \exp\left(\mathrm{j}\frac{2\pi}{N_y} nl\right), \tag{8}$$

where k, l are discrete spatial indices, m, n are discrete spatial frequency indices, N_x, N_y are the numbers of grid points in the x, y directions, $L_x = N_x\Delta$, $L_y = N_y\Delta$ are the lengths of the grid in the x, y directions in meters, and Δ is the grid spacing. In (8), r_x is an $N_y \times N_x$ grid of zero-mean, unit-variance circular complex Gaussian random numbers and Φ_{xx} is the spatial power spectrum of the x field component, i.e., the Fourier transform of μ_{xx}.

Note that (8) is the inverse Fourier transform of the product of two Fourier transforms (r_x and $\sqrt{\Phi_{xx}}$), and is physically equivalent to filtering white noise. Eq. (8) is in the form of a discrete inverse Fourier

transform, and therefore, we can use the fast Fourier transform algorithm to quickly realize T_x.

The moment μ_{xy} is formed by taking the cross-correlation of (8) with T_y, namely,

$$\begin{aligned}\langle T_x[k_1, l_1]T_y^*[k_2, l_2]\rangle =& \sum_{m_1}\sum_{n_1}\sum_{m_2}\sum_{n_2}\frac{\langle r_x[m_1, n_1]r_y^*[m_2, n_2]\rangle}{2L_xL_y}\sqrt{\Phi_{xx}[m_1, n_1]\Phi_{yy}[m_2, n_2]}\\ &\times\exp\left(\mathrm{j}\tfrac{2\pi}{N_x}m_1k_1\right)\exp\left(\mathrm{j}\tfrac{2\pi}{N_y}n_1l_1\right)\exp\left(-\mathrm{j}\tfrac{2\pi}{N_x}m_2k_2\right)\exp\left(-\mathrm{j}\tfrac{2\pi}{N_y}n_2l_2\right).\end{aligned} \tag{9}$$

The moment $\langle r_x[m_1, n_1]r_y^*[m_2, n_2]\rangle = 2\Gamma\delta[m_1 - m_2]\delta[n_1 - n_2]$, where Γ is the correlation coefficient between the r_x and r_y random numbers and $\delta[n]$ is the discrete Dirac delta function. This simplifies (9) to

$$\begin{aligned}\langle T_x[k_1, l_1]T_y^*[k_2, l_2]\rangle =& \sum_m\sum_n \Gamma\sqrt{\Phi_{xx}[m, n]\Phi_{yy}[m, n]}\\ &\times\frac{1}{L_xL_y}\exp\left[\mathrm{j}\frac{2\pi}{N_x}m(k_1 - k_2)\right]\exp\left[\mathrm{j}\frac{2\pi}{N_y}n(l_1 - l_2)\right].\end{aligned} \tag{10}$$

Recall from (4) that $\mu_{ij}(\boldsymbol{\rho}_1 - \boldsymbol{\rho}_2) = \langle T_i(\boldsymbol{\rho}_1)T_j^*(\boldsymbol{\rho}_2)\rangle$. For this to be true, $\Gamma\sqrt{\Phi_{xx}\Phi_{yy}}$ in (10) must equal Φ_{xy}. In practice, this means that the "self" power spectra set the cross-power spectrum, and subsequently, we can only simultaneously control two of the four polarization parameters, e.g., the intensity plus the degree of polarization or the intensity plus the ellipticity angle. We discuss this further below.

Before proceeding to the next topic, we substitute the above result into (7) as it will be useful in the analysis to follow:

$$\begin{aligned}W_{ij}(\boldsymbol{\rho}, \boldsymbol{\rho}, z) =& \frac{C_iC_j^*}{(\lambda z)^2}\mathcal{A}(0)\Gamma_{ij}\sqrt{\Phi_{xx}\left(\frac{\boldsymbol{\rho}}{\lambda z}\right)\Phi_{yy}\left(\frac{\boldsymbol{\rho}}{\lambda z}\right)}\\ \Gamma_{ij} =& \begin{cases}1 & i = j\\ 0 \leqslant \Gamma \leqslant 1 & i \neq j\end{cases}.\end{aligned} \tag{11}$$

For convenience, we let

$$\hat{\Phi}_{ii}\left(\frac{\boldsymbol{\rho}}{\lambda z}\right) = \frac{|C_i|^2\mathcal{A}(0)}{(\lambda z)^2}\Phi_{ii}\left(\frac{\boldsymbol{\rho}}{\lambda z}\right) \tag{12}$$

transforming (11) to

$$W_{ij}(\boldsymbol{\rho}, \boldsymbol{\rho}, z) = \exp[\mathrm{j}(\theta_x - \theta_y)]\Gamma_{ij}\sqrt{\hat{\Phi}_{xx}\left(\frac{\boldsymbol{\rho}}{\lambda z}\right)\hat{\Phi}_{yy}\left(\frac{\boldsymbol{\rho}}{\lambda z}\right)}, \tag{13}$$

where $\theta_i = \arg(C_i)$.

Far-zone polarization control

Here, in the second half of Section "Theory", we present the analytical details of controlling the far-zone beam's shape and polarization. We also discuss what characteristics of the far-zone beam can be controlled. We begin by introducing the far-zone Stokes and Poincaré sphere parameters, and derive expressions for them in terms of the self-power spectra introduced above.

Polarization parameters

With (13), we can derive relations for the far-zone Stokes and Poincaré sphere parameters in terms of $\hat{\Phi}_{xx}$ and $\hat{\Phi}_{yy}$. The Stokes parameters in terms of the CSD matrix elements and Poincaré sphere parameters are

$$\begin{aligned}S_0(\boldsymbol{\rho}, z) =& W_{xx}(\boldsymbol{\rho}, \boldsymbol{\rho}, z) + W_{yy}(\boldsymbol{\rho}, \boldsymbol{\rho}, z)\\ S_1(\boldsymbol{\rho}, z) =& W_{xx}(\boldsymbol{\rho}, \boldsymbol{\rho}, z) - W_{yy}(\boldsymbol{\rho}, \boldsymbol{\rho}, z)\\ =& S_0(\boldsymbol{\rho}, z)\mathcal{P}(\boldsymbol{\rho}, z)\cos[2\psi(\boldsymbol{\rho}, z)]\cos[2\chi(\boldsymbol{\rho}, z)]\\ S_2(\boldsymbol{\rho}, z) =& W_{xy}(\boldsymbol{\rho}, \boldsymbol{\rho}, z) + W_{yx}(\boldsymbol{\rho}, \boldsymbol{\rho}, z)\\ =& S_0(\boldsymbol{\rho}, z)\mathcal{P}(\boldsymbol{\rho}, z)\sin[2\psi(\boldsymbol{\rho}, z)]\cos[2\chi(\boldsymbol{\rho}, z)]\\ S_3(\boldsymbol{\rho}, z) =& \mathrm{j}[W_{yx}(\boldsymbol{\rho}, \boldsymbol{\rho}, z) - W_{xy}(\boldsymbol{\rho}, \boldsymbol{\rho}, z)]\\ =& S_0(\boldsymbol{\rho}, z)\mathcal{P}(\boldsymbol{\rho}, z)\sin[2\chi(\boldsymbol{\rho}, z)],\end{aligned} \tag{14}$$

where S_0 is the total average intensity, $0 \leqslant \mathcal{P} \leqslant 1$ is the degree of polarization, $-\pi/2 < \psi \leqslant \pi/2$ is the angle of polarization, and $-\pi/4 \leqslant \chi \leqslant \pi/4$ is the ellipticity angle [4,29,35]. For brevity, we drop the functional dependencies of the Stokes parameters, Poincaré sphere parameters, and CSD matrix elements. Henceforth, their dependence on $\boldsymbol{\rho}$ and z is assumed and suppressed. Substituting (13) into the above expressions and simplifying yields

$$\begin{aligned}S_0 =& \hat{\Phi}_{xx} + \hat{\Phi}_{yy}\\ S_1 =& \hat{\Phi}_{xx} - \hat{\Phi}_{yy} = S_0\mathcal{P}\cos(2\psi)\cos(2\chi)\\ S_2 =& 2\cos(\theta_x - \theta_y)\Gamma\sqrt{\hat{\Phi}_{xx}\hat{\Phi}_{yy}} = S_0\mathcal{P}\sin(2\psi)\cos(2\chi)\\ S_3 =& 2\sin(\theta_x - \theta_y)\Gamma\sqrt{\hat{\Phi}_{xx}\hat{\Phi}_{yy}} = S_0\mathcal{P}\sin(2\chi).\end{aligned} \tag{15}$$

In this form, it is clear that only two polarization parameters can be controlled at a time. It turns out that only S_0 and one other parameter can be controlled—the others $\mathcal{P}$, ψ, and χ are dependent on each other. In the next three sections, we derive equations for $\hat{\Phi}_{xx}$ and $\hat{\Phi}_{yy}$ in terms of S_0 and $\mathcal{P}$, S_0 and ψ, and S_0 and χ, respectively.

Controlling S_0 and $\mathcal{P}$

The applicable expressions for S_0 and $\mathcal{P}$ are

$$\begin{aligned}S_0 =& \hat{\Phi}_{xx} + \hat{\Phi}_{yy}\\ \mathcal{P} =& \frac{\sqrt{S_1^2 + S_2^2 + S_3^2}}{S_0} = \frac{\sqrt{(\hat{\Phi}_{xx} - \hat{\Phi}_{yy})^2 + 4\Gamma^2\hat{\Phi}_{xx}\hat{\Phi}_{yy}}}{\hat{\Phi}_{xx} + \hat{\Phi}_{yy}}.\end{aligned} \tag{16}$$

Solving the S_0 equation for $\hat{\Phi}_{yy}$, substituting the resulting expression into $\mathcal{P}$, and solving for $\hat{\Phi}_{xx}$ produces

$$4(1 - \Gamma^2)\hat{\Phi}_{xx}^2 - 4S_0(1 - \Gamma^2)\hat{\Phi}_{xx} + S_0^2(1 - \mathcal{P}^2) = 0. \tag{17}$$

Using the quadratic equation yields the desired result:

$$\begin{aligned}\hat{\Phi}_{xx} =& \tfrac{1}{2}S_0\left(1 \pm \sqrt{1 - \tfrac{1 - \mathcal{P}^2}{1 - \Gamma^2}}\right)\\ \hat{\Phi}_{yy} =& S_0 - \hat{\Phi}_{xx} = \tfrac{1}{2}S_0\left(1 \mp \sqrt{1 - \tfrac{1 - \mathcal{P}^2}{1 - \Gamma^2}}\right).\end{aligned} \tag{18}$$

Since both $\hat{\Phi}_{xx}$ and $\hat{\Phi}_{yy}$ must be real and positive, $\mathcal{P} \geqslant \Gamma$. Thus, $\mathcal{P}$'s minimum value is set by Γ. This means that $\Gamma < 1$ or $\mathcal{P}$ cannot be controlled.

Both roots in (18) are physical. The "+" root of $\hat{\Phi}_{xx}$ (hereafter referred to as just the "+" root) corresponds to the case when $\hat{\Phi}_{xx} > \hat{\Phi}_{yy}$, $S_1 > 0$, and the beam is polarized predominately in the horizontal direction. The "−" root of $\hat{\Phi}_{xx}$ (hereafter referred to as just the "−" root) corresponds to the opposite case—$\hat{\Phi}_{xx} < \hat{\Phi}_{yy}$, $S_1 < 0$, and the beam is polarized predominately in the vertical direction. Since S_1 is squared in (16), the root choice is irrelevant and both produce the desired S_0 and $\mathcal{P}$. Note that the root choice does affect the associated ψ, but we are not concerned with that quantity here.

Controlling S_0 and ψ

The applicable expressions for S_0 and ψ are

$$\begin{aligned}S_0 =& \hat{\Phi}_{xx} + \hat{\Phi}_{yy}\\ \frac{\sin(2\psi)}{\cos(2\psi)} =& \frac{S_2}{S_1} = \frac{2\Gamma\cos(\theta_x - \theta_y)\sqrt{\hat{\Phi}_{xx}\hat{\Phi}_{yy}}}{\hat{\Phi}_{xx} - \hat{\Phi}_{yy}}.\end{aligned} \tag{19}$$

Solving the S_0 equation for $\hat{\Phi}_{yy}$, substituting the resulting expression into $\tan(2\psi)$, and solving for $\hat{\Phi}_{xx}$ produces

$$4(S_\psi^2 + \Gamma^2C_\theta^2C_\psi^2)\hat{\Phi}_{xx}^2 - 4S_0(S_\psi^2 + \Gamma^2C_\theta^2C_\psi^2)\hat{\Phi}_{xx} + S_0^2S_\psi^2 = 0, \tag{20}$$

where $S_\psi = \sin(2\psi)$, $C_\psi = \cos(2\psi)$, and $C_\theta = \cos(\theta_x - \theta_y)$. Again, applying the quadratic equation and simplifying yields the final result:

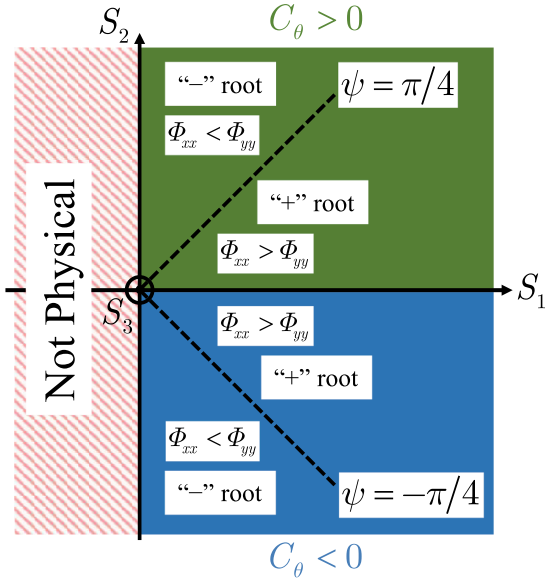

Fig. 1. S_1-S_2 plane showing the physically realizable values of ψ.

$$\hat{\Phi}_{xx} = \frac{1}{2}S_0\left(1 \pm \sqrt{1 - \frac{S_\psi^2}{S_\psi^2 + \Gamma^2 C_\theta^2 C_\psi^2}}\right)$$
$$\hat{\Phi}_{yy} = S_0 - \hat{\Phi}_{xx} = \frac{1}{2}S_0\left(1 \mp \sqrt{1 - \frac{S_\psi^2}{S_\psi^2 + \Gamma^2 C_\theta^2 C_\psi^2}}\right). \tag{21}$$

There are several aspects of (21) that warrant discussion. If $\Gamma = 0$, then $\hat{\Phi}_{xx} = \hat{\Phi}_{yy} = S_0/2$. This situation physically corresponds to unpolarized light, and ψ is undefined. Thus, $\Gamma > 0$ or ψ cannot be controlled.

A similar thing happens when $\theta_x - \theta_y = \pm m\pi/2$, where m is an odd integer. Here again, $\hat{\Phi}_{xx} = \hat{\Phi}_{yy} = S_0/2$; however, in this situation, the resulting beam is circularly polarized. When it comes to controlling ψ, circular polarization is no different than random polarization, and $\theta_x - \theta_y \neq \pm m\pi/2$ or ψ cannot be controlled.

Lastly, inspection of (19) reveals that the signs of $\hat{\Phi}_{xx} - \hat{\Phi}_{yy}$ and C_θ determine the range of physically meaningful (or possible) values of ψ. Fig. 1 shows how these signs affect the range of ψ. The figure depicts ψ in the S_1-S_2 plane. The polarization angle ψ is physically limited to $(-\pi/2, \pi/2]$. For $|\psi| < \pi/4$, the beam is more horizontally polarized than vertically polarized. This corresponds to positive S_1, $\hat{\Phi}_{xx} > \hat{\Phi}_{yy}$, and the "+" root in (21). For $|\psi| > \pi/4$, the opposite is true: the beam is more vertically polarized than horizontally polarized, $S_1 < 0$, $\hat{\Phi}_{xx} < \hat{\Phi}_{yy}$, and the "−" root in (21) is applicable. These are labeled in Fig. 1 as well as the special angles $\psi = \pm\pi/4$.

The sign of C_θ—$\mathrm{sgn}(C_\theta)$, where $\mathrm{sgn}(x)$ is the signum function—determines whether ψ is restricted to the upper or lower quadrant of the right-half S_1-S_2 plane. When $\mathrm{sgn}(C_\theta) = 1$, the physically possible values of ψ are between $[0, \pi/2]$. This corresponds to the green region in Fig. 1. When $\mathrm{sgn}(C_\theta) = -1$, ψ can take on the values in the blue region, namely, $\psi \in (-\pi/2, 0]$.

The utility of Fig. 1 is best illustrated through an example. Let $\Gamma = 0.5$ and $\theta_x - \theta_y = -2\pi/3$. We want to generate a vector Schell-model source that radiates a beam with an S_0 and ψ that are grayscale images, which are arbitrarily scaled. The S_0 image scale is irrelevant; however, the ψ image must be mapped to a set of values that are physically possible given $\mathrm{sgn}(C_\theta)$. Here, $\mathrm{sgn}(C_\theta) = -1$, the blue region in Fig. 1 is applicable, and the ψ image values should be mapped to $(-\pi/2, 0]$. For all values of the ψ image less than $-\pi/4$, the "−" root in (21) should be chosen; for all values greater than $-\pi/4$, the "+" root in (21) should be chosen.

Controlling S_0 and χ

The applicable expressions for S_0 and χ are

$$S_0 = \hat{\Phi}_{xx} + \hat{\Phi}_{yy}$$
$$\frac{\sin(2\chi)}{\cos(2\chi)} = \frac{S_3}{\sqrt{S_1^2 + S_2^2}} = \frac{2\Gamma\sin(\theta_x - \theta_y)\sqrt{\hat{\Phi}_{xx}\hat{\Phi}_{yy}}}{\sqrt{(\hat{\Phi}_{xx} - \hat{\Phi}_{yy})^2 + 4\Gamma^2\cos^2(\theta_x - \theta_y)\hat{\Phi}_{xx}\hat{\Phi}_{yy}}}. \tag{22}$$

Solving the S_0 equation for $\hat{\Phi}_{yy}$, substituting the resulting expression into $\tan(2\chi)$, and solving for $\hat{\Phi}_{xx}$ produces

$$4(S_\chi^2 - \Gamma^2 C_\theta^2 S_\chi^2 + \Gamma^2 S_\theta^2 C_\chi^2)\hat{\Phi}_{xx}^2 - 4S_0(S_\chi^2 - \Gamma^2 C_\theta^2 S_\chi^2 + \Gamma^2 S_\theta^2 C_\chi^2)\hat{\Phi}_{xx} + S_0^2 S_\chi^2 = 0, \tag{23}$$

where $S_\chi = \sin(2\chi)$, $C_\chi = \cos(2\chi)$, $C_\theta = \cos(\theta_x - \theta_y)$, and $S_\theta = \sin(\theta_x - \theta_y)$. Once again using the quadratic equation and simplifying yields the final result:

$$\hat{\Phi}_{xx} = \frac{1}{2}S_0\left(1 \pm \sqrt{1 - \frac{S_\chi^2}{S_\chi^2 - \Gamma^2 C_\theta^2 S_\chi^2 + \Gamma^2 S_\theta^2 C_\chi^2}}\right)$$
$$\hat{\Phi}_{yy} = S_0 - \hat{\Phi}_{xx} = \frac{1}{2}S_0\left(1 \mp \sqrt{1 - \frac{S_\chi^2}{S_\chi^2 - \Gamma^2 C_\theta^2 S_\chi^2 + \Gamma^2 S_\theta^2 C_\chi^2}}\right). \tag{24}$$

Like the S_0 and $\mathcal{P}$ section above, both the "+" and "−" roots in (24) are physical and correspond to the same scenarios described therein. Since S_1 is squared in (22), the root choice is again irrelevant and both produce the desired S_0 and χ.

Exactly the same as when controlling S_0 and ψ, $\Gamma > 0$ or χ cannot be controlled. $\Gamma = 0$ corresponds to unpolarized light, and χ has no physical meaning.

Lastly, since $\hat{\Phi}_{xx}$ and $\hat{\Phi}_{yy}$ must be real and positive, $S_\chi^2 \geqslant S_\chi^2 - \Gamma^2 C_\theta^2 S_\chi^2 + \Gamma^2 S_\theta^2 C_\chi^2$. Simplifying this relation leads to the inequality $S_\chi \leqslant S_\theta$. The ellipticity angle χ is physically limited to $[-\pi/4, \pi/4]$, and therefore, $|\chi| \leqslant |\arcsin(S_\theta)/2|$. Thus, $|\chi|$'s maximum value is set by the value of $\theta_x - \theta_y$ wrapped into the region $[-\pi/2, \pi/2]$. The sign of S_θ, $\mathrm{sgn}(S_\theta)$, determines whether the resulting beam is right-hand circular or left-hand circular polarization dominant—positive in the former case, negative in the latter.

Fig. 2 shows how $\mathrm{sgn}(S_\theta)$ affects the physically meaningful (or possible) values of χ. The figure shows the S_2-S_3 plane; the picture in the S_1-S_3 plane is identical. As already stated, χ must be between $[-\pi/4, \pi/4]$, hence the solid lines at those angles. χ is further bounded by the values $\pm|\arcsin(S_\theta)/2|$, which are represented on the figure as dashed lines. As an example, assume that $\mathrm{sgn}(S_\theta) = -1$. This corresponds to the blue region in Fig. 2 and shows that

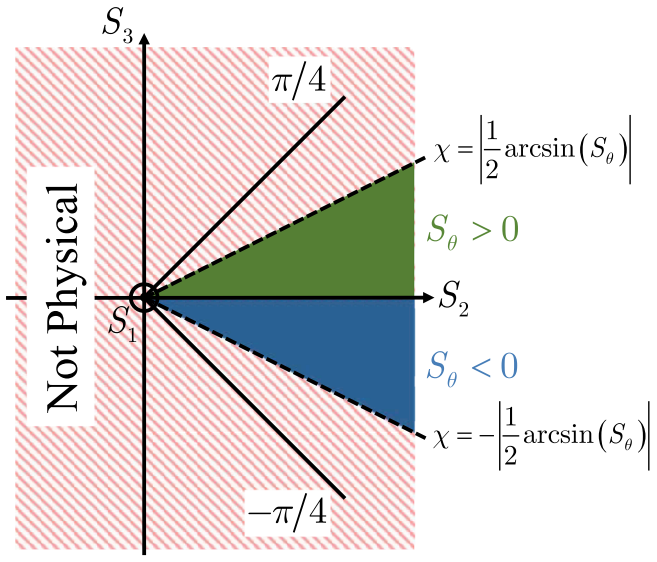

Fig. 2. S_2-S_3 plane showing the physically realizable values of χ.

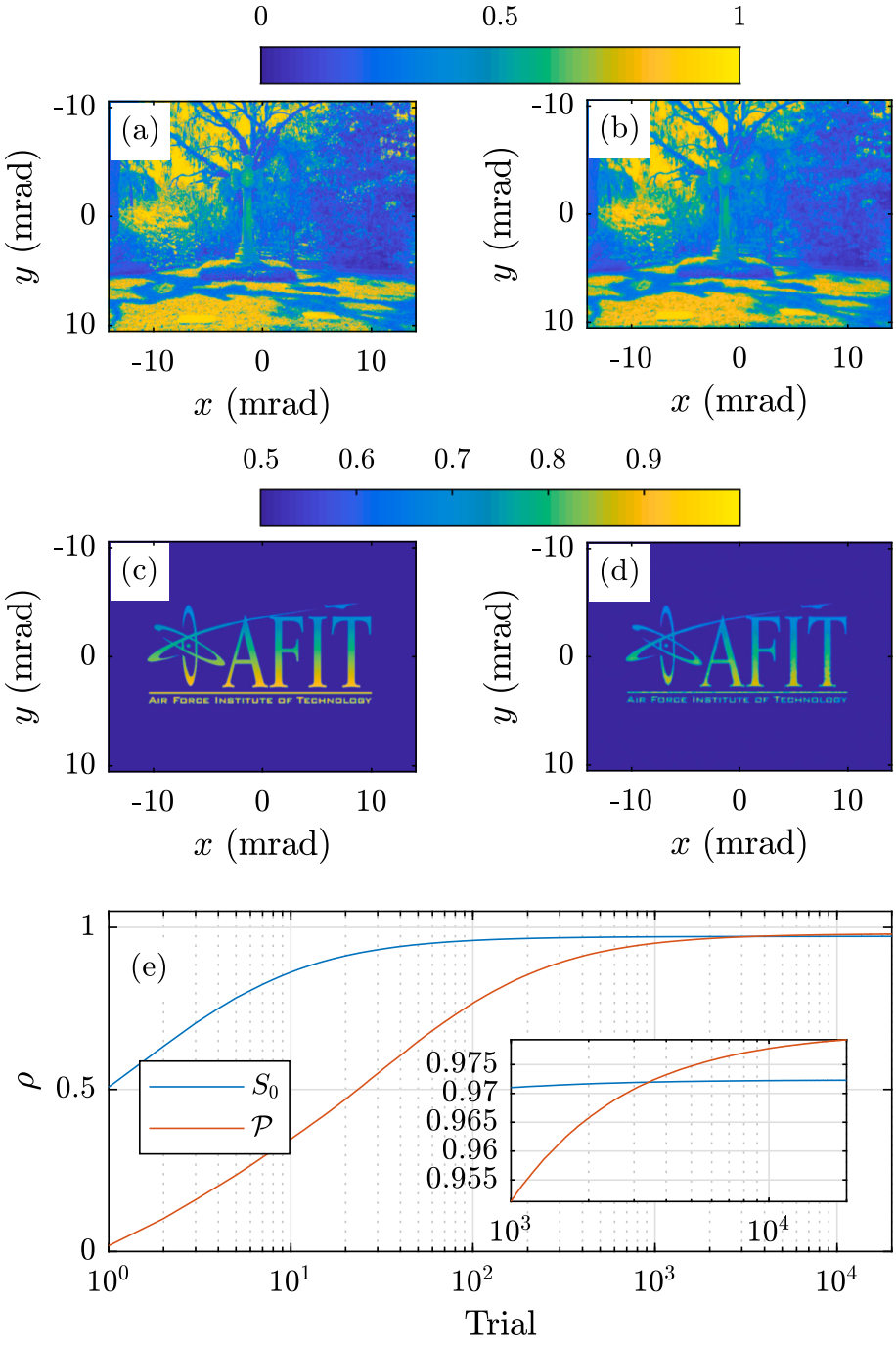

Fig. 3. Simulation results demonstrating control of S_0 and $\mathcal{P}$—(a) desired (or truth) S_0, (b) simulated S_0, (c) desired (or truth) $\mathcal{P}$, (d) simulated $\mathcal{P}$, and (e) cumulative correlation coefficients ρ of the simulated S_0 (blue trace) and $\mathcal{P}$ (red trace) with their associated desired quantities versus Monte-Carlo trial number. The inset in (e) shows a "close-up" view of ρ from trials 1000–20,000. (For interpretation of the references to colour in this figure legend, the reader is referred to the web version of this article.)

$\chi \in [-|\arcsin(S_\theta)/2|, 0]$. The green region in Fig. 2 is associated with $\text{sgn}(S_\theta) = 1$.

To illustrate the utility of Fig. 2, we refer back to the example discussed in the S_0 and ψ section. Let $\Gamma = 0.5$ and $\theta_x - \theta_y = -2\pi/3$. Our goal is to generate a vector Schell-model source that radiates a beam with an S_0 and χ that are grayscale images, which are arbitrarily scaled. Again, the scale of the S_0 image is irrelevant. The χ image must be mapped to a set of values that are physically possible given $\text{sgn}(S_\theta)$. Here, $\text{sgn}(S_\theta) = -1$, the blue region in Fig. 2 is applicable, and the χ image values should be mapped to $[-|\arcsin(S_\theta)/2|, 0]$. As previously discussed, the root choice in (24) is irrelevant.

Theory summary

In summary, to produce a vector Schell-model source that radiates a beam with a desired shape and polarization properties.

1. Choose C_x, C_y, Γ, and $A(\boldsymbol{\rho})$. To some extent, these parameters can be used to control the beam shape and polarization in the source plane. Recall that Γ, $\arg(C_x)$, and $\arg(C_y)$ affect the polarization state in the far zone.
2. Choose the desired S_0 and $\mathcal{P}$, ψ, or χ images.
3. Use (18), (21), or (24) (whichever is applicable) to find $\hat{\Phi}_{xx}$ and $\hat{\Phi}_{yy}$.

(a) For controlling S_0 and $\mathcal{P}$, the values of the desired $\mathcal{P}$ image should be mapped into the range $[\Gamma, 1]$.
(b) For controlling S_0 and ψ, use Fig. 1 to determine the values to which the desired ψ image should be mapped.
(c) For controlling S_0 and χ, use Fig. 2 to determine the values to which the desired χ image should be mapped.

4. Use a multivariate Gaussian random number generator to produce correlated r_x and r_y. The means and covariance matrix are

$$\begin{aligned}
&\langle r_x^{\mathrm{r}}\rangle = \langle r_x^{\mathrm{i}}\rangle = \langle r_y^{\mathrm{r}}\rangle = \langle r_y^{\mathrm{i}}\rangle = 0\\
&\Sigma = \begin{bmatrix} \langle (r_x^{\mathrm{r}})^2\rangle & \langle r_x^{\mathrm{r}} r_x^{\mathrm{i}}\rangle & \langle r_x^{\mathrm{r}} r_y^{\mathrm{r}}\rangle & \langle r_x^{\mathrm{r}} r_y^{\mathrm{i}}\rangle \\ \langle r_x^{\mathrm{i}} r_x^{\mathrm{r}}\rangle & \langle (r_x^{\mathrm{i}})^2\rangle & \langle r_x^{\mathrm{i}} r_y^{\mathrm{r}}\rangle & \langle r_x^{\mathrm{i}} r_y^{\mathrm{i}}\rangle \\ \langle r_y^{\mathrm{r}} r_x^{\mathrm{r}}\rangle & \langle r_y^{\mathrm{r}} r_x^{\mathrm{i}}\rangle & \langle (r_y^{\mathrm{r}})^2\rangle & \langle r_y^{\mathrm{r}} r_y^{\mathrm{i}}\rangle \\ \langle r_y^{\mathrm{i}} r_x^{\mathrm{r}}\rangle & \langle r_y^{\mathrm{i}} r_x^{\mathrm{i}}\rangle & \langle r_y^{\mathrm{i}} r_y^{\mathrm{r}}\rangle & \langle (r_y^{\mathrm{i}})^2\rangle \end{bmatrix} = \begin{bmatrix} 1 & 0 & \Gamma & 0 \\ 0 & 1 & 0 & \Gamma \\ \Gamma & 0 & 1 & 0 \\ 0 & \Gamma & 0 & 1 \end{bmatrix}\\
&r_x = r_x^{\mathrm{r}} + \mathrm{j} r_x^{\mathrm{i}}\\
&r_y = r_y^{\mathrm{r}} + \mathrm{j} r_y^{\mathrm{i}},
\end{aligned} \tag{25}$$

where the superscripts "r" and "i" stand for real and imaginary parts, respectively.

5. Use (8) to generate instances of T_x and T_y. Recall that Φ_{xx} and Φ_{yy} are related to $\hat{\Phi}_{xx}$ and $\hat{\Phi}_{yy}$ by (12).
6. Use (2) to generate a vector Schell-model source field realization.
7. Synthesize field realization using spatial light modulators [2,3,15,19–21].

We demonstrate and validate the use of the above procedure via simulation in the next section.

Validation

Here, we perform Monte-Carlo wave-optics simulations to validate the analysis of the previous section. Before proceeding to the results, we discuss the simulation particulars so that the interested reader can reproduce our results, or perform a similar simulation for their own purposes.

Simulation description

For these simulations, we used computational grids that were $N_x = N_y = 1024$ points on a side with grid spacings $\Delta = 15$ μm. The simulated source plane field was

$$\boldsymbol{E}(\boldsymbol{\rho}) = \mathrm{rect}\left(\frac{x}{D}\right)\mathrm{rect}\left(\frac{y}{D}\right)\left[\hat{\boldsymbol{x}}\exp\left(-\mathrm{j}\frac{2\pi}{3}\right)T_x(\boldsymbol{\rho}) + \hat{\boldsymbol{y}}\,T_y(\boldsymbol{\rho})\right], \tag{26}$$

where $D = 7.68$ mm and $\mathrm{rect}(x)$ was [36]

$$\mathrm{rect}(x) = \begin{cases} 1 & |x| < 1/2 \\ 1/2 & |x| = 1/2 \\ 0 & \text{otherwise} \end{cases}. \tag{27}$$

The rectangular shape and D were chosen to correspond with a popular model of liquid crystal spatial light modulator [37]. The simulated wavelength was $\lambda = 632.8$ nm.

The T_x and T_y were generated following the procedure in Section "Theory summary". The desired S_0 was the Celtic cross image shown in Figs. 3–5(a); the desired $\mathcal{P}$, ψ, and χ were the Air Force Institute of Technology logo shown in Figs. 3–5(c), respectively. Recall that to control $\mathcal{P}$, $\Gamma < 1$ and to control ψ or χ, $\Gamma > 0$. Here, we arbitrarily chose $\Gamma = 0.5$.

We generated 20,000 realizations of the vector field in (26) and propagated each to the far field using fast Fourier transforms [38,39]. We then computed the far-zone, single-point CSD matrix elements and, from these, computed the Stokes and Poincaré sphere parameters using (14). We lastly compared the simulated S_0 and $\mathcal{P}$, ψ, or χ to the desired images. We performed the simulations using MATLAB® version R2017a; the scripts (.m files) are included as supplementary materials.

Results and discussion

Figs. 3–5 show the S_0 and $\mathcal{P}$, S_0 and ψ, and S_0 and χ results, respectively. The figures are organized as follows: (a) and (c) show the desired S_0 and $\mathcal{P}$, ψ, or χ (whichever is applicable), respectively. Subfigures (b) and (d) show the corresponding simulated results. Lastly, (e) shows the cumulative two-dimensional correlation coefficients ρ of the simulated S_0 and $\mathcal{P}$, ψ, or χ (whichever is applicable) with their corresponding desired images versus trial number. The inset shows a "close-up" view of ρ from trials 1000–20,000. Figs. 3–5(a) and (b), the S_0 images, are plotted on the same false color scale $[0, 1]$ shown in the color bars above subfigures (a) and (b). Figs. 3(c) and (d), 4(c) and (d), and 5(c) and (d) are plotted on false color scales $[\Gamma, 1] = [0.5, 1]$, $[-\pi/2, 0]$, and $[-|\arcsin(S_6)/2|, 0] = [-\pi/6, 0]$, respectively.

The agreement between the desired images and the simulated results is very good. The results in Figs. 3–5 validate the theoretical analysis presented in Section "Theory".

The simulated S_0 and $\mathcal{P}$, ψ, or χ converge to their asymptotic values within approximately 1000 trials. The ρ in Figs. 3–5(e) asymptote at approximately the same level, i.e., between 0.97 and 0.984. These numbers are not likely to appreciably increase, even with running many more trials, because of a theoretical assumption we made in Section "Theory".

Recall (6), which is rewritten below for the reader's convenience:

$$W_{ij}(\boldsymbol{\rho}, \boldsymbol{\rho}, z) = S_{ij}(\boldsymbol{\rho}, z) = \frac{C_i C_j^*}{(\lambda z)^2}\iint_{-\infty}^{\infty}\mu_{ij}(\boldsymbol{t})\mathcal{A}(\boldsymbol{t})\exp\left(-\mathrm{j}\frac{k}{z}\boldsymbol{t}\cdot\boldsymbol{\rho}\right)\mathrm{d}^2 t. \tag{28}$$

In the analysis, we assumed that the partially coherent source was a quasi-homogeneous electromagnetic source. In other words, we assumed that $\mathcal{A}$ (the autocorrelation of the source's shape) was much broader than μ_{ij}, such that $\mathcal{A}$ could be evaluated at $\boldsymbol{t} = 0$ and removed from the integral, leaving S_{ij} being (approximately) proportional to the spatial cross-power spectrum Φ_{ij} (or equivalently, the spatial Fourier transform of μ_{ij}). This assumption was necessary to derive the closed-form expressions later in Section "Theory" that comprised the main contributions of this paper.

Although it is not possible to derive the expressions presented in the latter half of Section "Theory" and include source shape, we can gain a physical understanding of how source shape affects S_0 and $\mathcal{P}$, ψ, or χ by examining (28) more closely. Eq. (28) is the Fourier transform of the product of two functions. By the convolution theorem, (28) is equivalent to the convolution of Φ_{ij} with the Fourier transform of $\mathcal{A}$ (hereafter, $\tilde{\mathcal{A}}$). Thus, the true far-zone S_{ij} is a spatially filtered version of Φ_{ij}; the filter is $\tilde{\mathcal{A}}$. For broad, or slowly varying $\mathcal{A}$ (as assumed in Section "Theory"), $\tilde{\mathcal{A}}$ is narrow or fast, and in the asymptotic limit, S_{ij} is proportional to Φ_{ij}. For narrow or fast $\mathcal{A}$, $\tilde{\mathcal{A}}$ is broad or slow, and S_{ij} is proportional to $\tilde{\mathcal{A}}$ in that asymptotic limit.

The simulated results include the effects of source shape [recall the simulated source field in (26)]. Thus, the above discussion explains the ρ results in Figs. 3–5(e). It also explains the minor qualitative differences in Figs. 3–5(a) and (b), and (c) and (d). More importantly, the above discussion provides the user with a physical understanding of the actual, true performance of the beam shaping technique developed in this paper.

Conclusion

In this paper, we developed a method using a vector Schell-model source to control the far-zone beam shape and polarization. This research extended prior scalar Schell-model source work which only controlled beam shape.

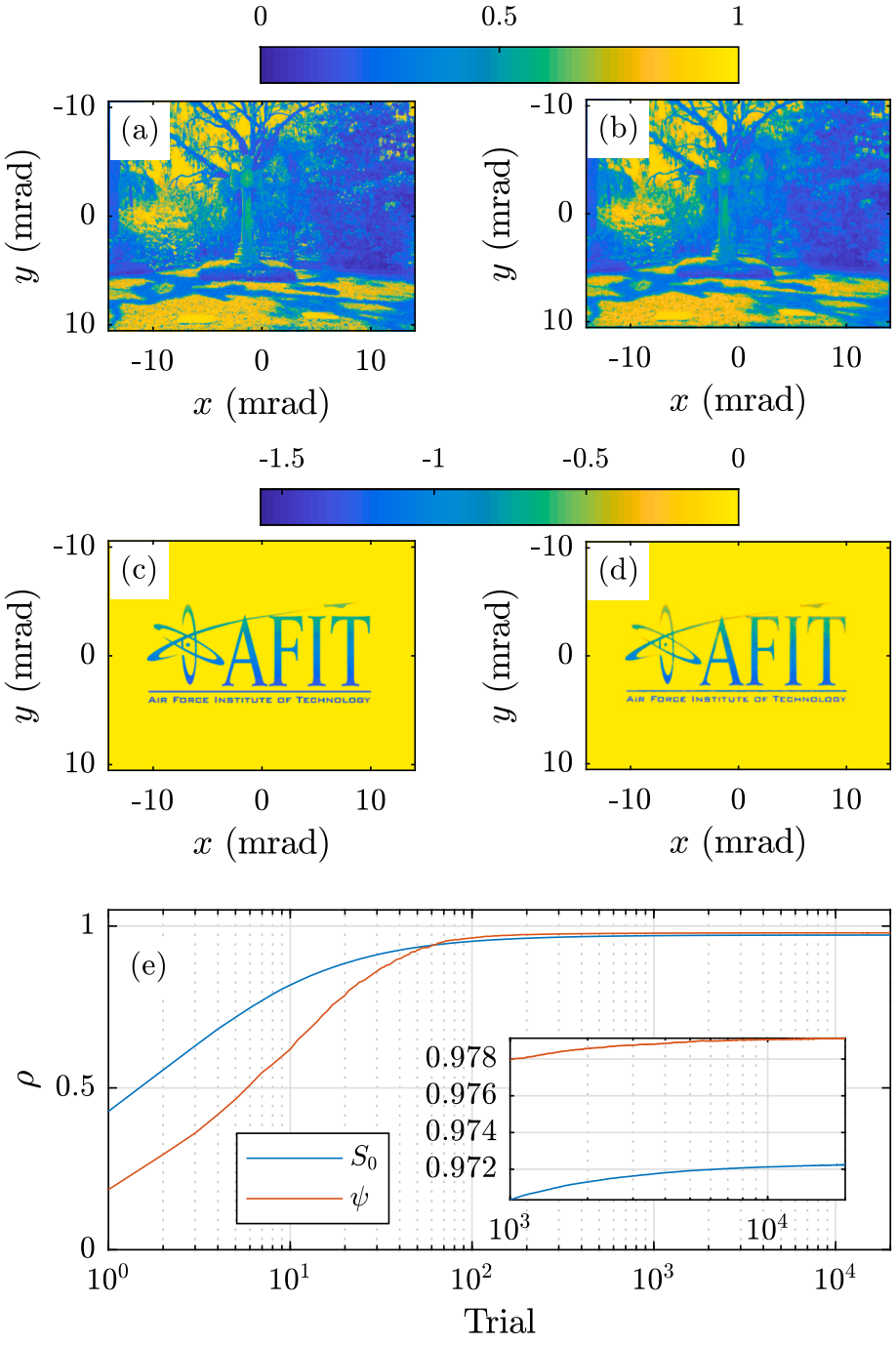

Fig. 4. Simulation results demonstrating control of S_0 and ψ—(a) desired (or truth) S_0, (b) simulated S_0, (c) desired (or truth) ψ, (d) simulated ψ, and (e) cumulative correlation coefficients ρ of the simulated S_0 (blue trace) and ψ (red trace) with their associated desired quantities versus Monte-Carlo trial number. The inset in (e) shows a "close-up" view of ρ from trials 1000–20,000. (For interpretation of the references to colour in this figure legend, the reader is referred to the web version of this article.)

By applying Fourier and statistical optics theory, we derived expressions for the vector power spectra, necessary to generate a vector Schell-model source that radiates a beam with designer far-zone shape and polarization properties. We discussed what aspects of the far-zone beam—S_0, $\mathcal{P}$, ψ, and χ—can be controlled. We also developed a step-by-step procedure that described how to synthesize random vector field instances with the proper statistics.

Lastly, we presented Monte-Carlo simulation results to validate our analysis. We successfully demonstrated the concept by generating vector Schell-model sources that radiated beams with shapes (S_0) and Poincaré sphere parameters ($\mathcal{P}$, ψ, or χ) that were complex grayscale images.

The beam-shaping method introduced in this paper will be useful in optical trapping, optical communications, directed energy, remote sensing, and medical applications.

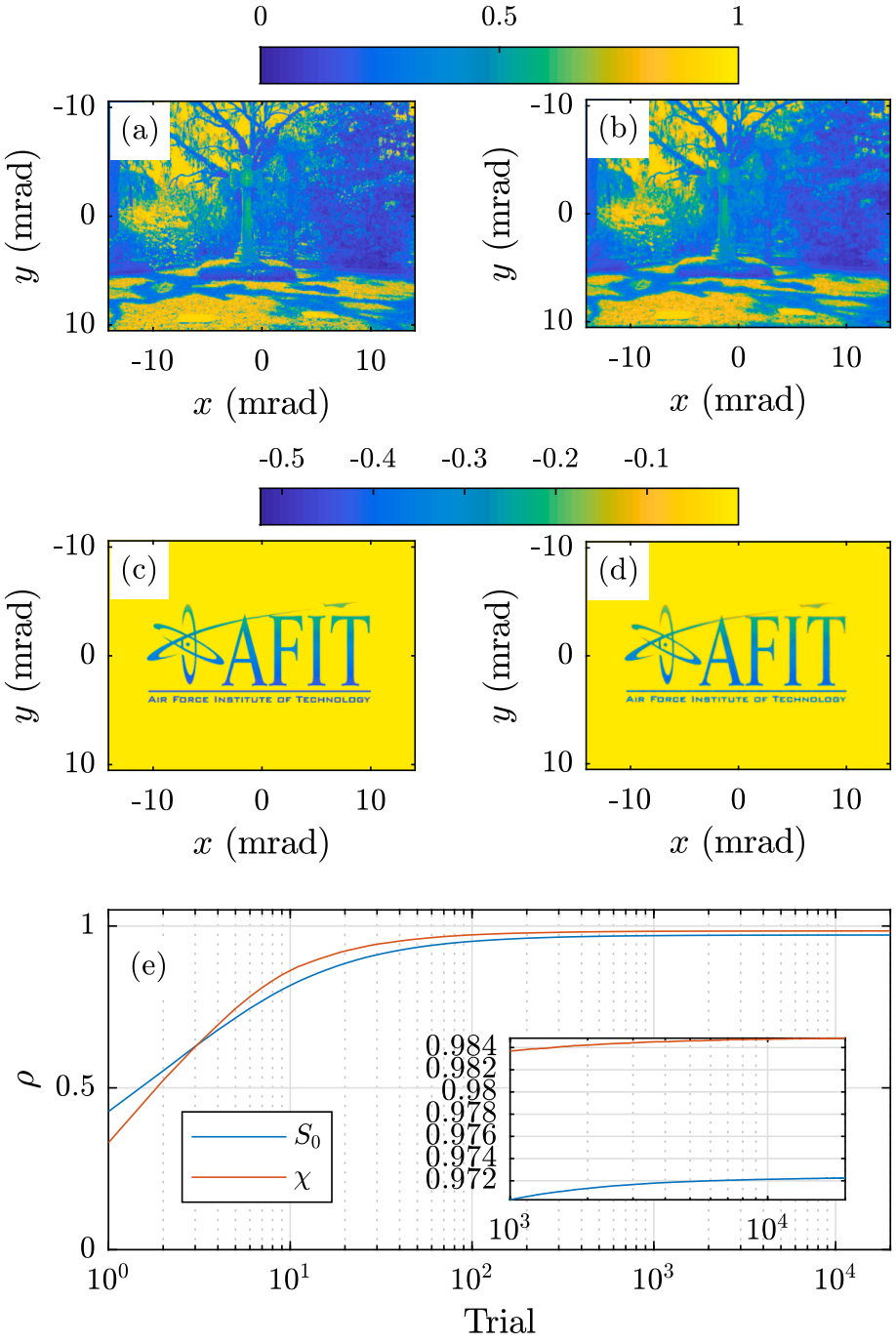

Fig. 5. Simulation results demonstrating control of S_0 and χ—(a) desired (or truth) S_0, (b) simulated S_0, (c) desired (or truth) χ, (d) simulated χ, and (e) cumulative correlation coefficients ρ of the simulated S_0 (blue trace) and χ (red trace) with their associated desired quantities versus Monte-Carlo trial number. The inset in (e) shows a "close-up" view of ρ from trials 1000–20,000. (For interpretation of the references to colour in this figure legend, the reader is referred to the web version of this article.)

Declarations of interest

None.

Appendix A. Supplementary material

Supplementary data associated with this article can be found, in the online version, at https://doi.org/10.1016/j.rinp.2019.02.008.

References

[1] Rubinsztein-Dunlop H, Forbes A, Berry MV, Dennis MR, Andrews DL, Mansuripur M, et al. Roadmap on structured light. J Opt 2017;19(1):013001 <http://stacks.iop.org/2040-8986/19/i=1/a=013001>.

[2] Rosales-Guzmán C, Ndagano B, Forbes A. A review of complex vector light fields and their applications. J Opt 2018;20(12):123001 <http://stacks.iop.org/2040-8986/20/i=12/a=123001>.

[3] Zhan Q, editor. Vectorial optical fields: fundamentals and applications. World Scientific; 2014.

[4] Korotkova O. Random light beams: theory and applications. Boca Raton, FL: CRC; 2014.

[5] Cai Y, Chen Y, Wang F. Generation and propagation of partially coherent beams with nonconventional correlation functions: a review. J Opt Soc Am A 2014;31(9):2083–96. https://doi.org/10.1364/JOSAA.31.002083.

[6] Mei Z, Korotkova O. Random sources for rotating spectral densities. Opt Lett 2017;42(2):255–8. https://doi.org/10.1364/OL.42.000255 <http://ol.osa.org/abstract.cfm?URI=ol-42-2-255>.

[7] Mei Z, Korotkova O. Electromagnetic Schell-model sources generating far fields

with stable and flexible concentric rings profiles. Opt Express 2016;24(5):5572–83. https://doi.org/10.1364/OE.24.005572<http://www.opticsexpress.org/abstract.cfm?URI=oe-24-5-5572>.
[8] Chen Y, Ponomarenko SA, Cai Y. Self-steering partially coherent beams. Sci Rep 2017;7:39957. https://doi.org/10.1038/srep39957.
[9] Chen Y, Gu J, Wang F, Cai Y. Self-splitting properties of a Hermite-Gaussian correlated Schell-model beam. Phys Rev A 2015;91:013823. https://doi.org/10.1103/PhysRevA.91.013823<http://link.aps.org/doi/10.1103/PhysRevA.91.013823>.
[10] Lajunen H, Saastamoinen T. Propagation characteristics of partially coherent beams with spatially varying correlations. Opt Lett 2011;36(20):4104–6. https://doi.org/10.1364/OL.36.004104<http://ol.osa.org/abstract.cfm?URI=ol-36-20-4104>.
[11] Liang C, Mi C, Wang F, Zhao C, Cai Y, Ponomarenko SA. Vector optical coherence lattices generating controllable far-field beam profiles. Opt Express 2017;25(9):9872–85. https://doi.org/10.1364/OE.25.009872<http://www.opticsexpress.org/abstract.cfm?URI=oe-25-9-9872>.
[12] Chen Y, Wang F, Yu J, Liu L, Cai Y. Vector Hermite-Gaussian correlated Schell-model beam. Opt Express 2016;24(14):15232–50. https://doi.org/10.1364/OE.24.015232<http://www.opticsexpress.org/abstract.cfm?URI=oe-24-14-15232>.
[13] Tong Z, Korotkova O. Electromagnetic nonuniformly correlated beams. J Opt Soc Am A 2012;29(10):2154–8. https://doi.org/10.1364/JOSAA.29.002154<http://josaa.osa.org/abstract.cfm?URI=josaa-29-10-2154>.
[14] Cai Y, Chen Y, Yu J, Liu X, Liu L. Generation of partially coherent beams. Prog Opt 2017;62:157–223. https://doi.org/10.1016/bs.po.2016.11.001<http://www.sciencedirect.com/science/article/pii/S0079663816300166>.
[15] Hyde MW, Bose-Pillai S, Voelz DG, Xiao X. Generation of vector partially coherent optical sources using phase-only spatial light modulators. Phys Rev Appl 2016;6:064030. https://doi.org/10.1103/PhysRevApplied. 6.064030<https://link.aps.org/doi/10.1103/PhysRevApplied.6.064030>.
[16] Ostrovsky AS, Martínez-Niconoff G, Arrizón V, Martínez-Vara P, Olvera-Santamaría MA, Rickenstorff-Parrao C. Modulation of coherence and polarization using liquid crystal spatial light modulators. Opt Express 2009;17(7):5257–64. https://doi.org/10.1364/OE.17.005257<http://www.opticsexpress.org/abstract.cfm?URI=oe-17-7-5257>.
[17] Shirai T, Wolf E. Coherence and polarization of electromagnetic beams modulated by random phase screens and their changes on propagation in free space. J Opt Soc Am A 2004;21(10):1907–16. https://doi.org/10.1364/JOSAA.21.001907<http://josaa.osa.org/abstract.cfm?URI=josaa-21-10-1907>.
[18] Shirai T, Korotkova O, Wolf E. A method of generating electromagnetic Gaussian Schell-model beams. J Opt A: Pure Appl Opt 2005;7(5):232–7<http://stacks.iop.org/1464-4258/7/i=5/a=004>.
[19] Chen Z, Zeng T, Qian B, Ding J. Complete shaping of optical vector beams. Opt Express 2015;23(14):17701–10. https://doi.org/10.1364/OE.23.017701<http://www.opticsexpress.org/abstract.cfm?URI=oe-23-14-17701>.
[20] Yu Z, Chen H, Chen Z, Hao J, Ding J. Simultaneous tailoring of complete polarization, amplitude and phase of vector beams. Opt Commun 2015;345:135–40. https://doi.org/10.1016/j.optcom.2015.02.008<http://www.sciencedirect.com/science/article/pii/S003040181500098X>.
[21] Rosales-Guzmán C, Bhebhe N, Forbes A. Simultaneous generation of multiple vector beams on a single SLM. Opt Express 2017;25(21):25697–706. https://doi.org/10.1364/OE.25.025697<http://www.opticsexpress.org/abstract.cfm?URI=oe-25-21-25697>.
[22] Fu S, Zhai Y, Wang T, Yin C, Gao C. Tailoring arbitrary hybrid Poincarè beams through a single hologram. Appl Phys Lett 2017;111(21):211101. https://doi.org/10.1063/1.5008954. arXiv: <https://doi.org/10.1063/1.5008954>.
[23] Rosales-Guzmán C, Bhebhe N, Mahonisi N, Forbes A. Multiplexing 200 modes on a single digital hologram, arXiv:<1706.06129>. <https://arxiv.org/abs/1706.06129>.
[24] Voelz D, Xiao X, Korotkova O. Numerical modeling of Schell-model beams with arbitrary far-field patterns. Opt Lett 2015;40(3):352–5. https://doi.org/10.1364/OL.40.000352<http://ol.osa.org/abstract.cfm?URI=ol-40-3-352>.
[25] Hyde IV MW, Basu S, Xiao X, Voelz DG. Producing any desired far-field mean irradiance pattern using a partially-coherent Schell-model source. J Opt 2015;17(5):055607. https://doi.org/10.1088/2040-8978/17/5/055607<http://stacks.iop.org/2040-8986/17/i=5/a=055607>.
[26] Hyde MW, Basu S, Voelz DG, Xiao X. Experimentally generating any desired partially coherent Schell-model source using phase-only control. J Appl Phys 2015;118(9):093102. https://doi.org/10.1063/1.4929811<http://scitation.aip.org/content/aip/journal/jap/118/9/10.1063/1.4929811>.
[27] Hyde IV MW, Basu S, Voelz DG, Xiao X. Generating partially coherent Schell-model sources using a modified phase screen approach. Opt. Eng. 2015;54(12):120501. https://doi.org/10.1117/1.OE.54.12.120501.
[28] Mandel L, Wolf E. Optical coherence and quantum optics. New York, NY: Cambridge University; 1995.
[29] Wolf E. Introduction to the theory of coherence and polarization of light. Cambridge, UK: Cambridge University; 2007.
[30] Korotkova O, Hoover BG, Gamiz VL, Wolf E. Coherence and polarization properties of far fields generated by quasi-homogeneous planar electromagnetic sources. J Opt Soc Am A 2005;22(11):2547–56. https://doi.org/10.1364/JOSAA.22.002547<http://josaa.osa.org/abstract.cfm?URI=josaa-22-11-2547>.
[31] Goodman JW. Statistical optics. 2nd ed. Hoboken, NJ: Wiley; 2015.
[32] Basu S, Hyde MW, Xiao X, Voelz DG, Korotkova O. Computational approaches for generating electromagnetic Gaussian Schell-model sources. Opt Express 2014;22(26):31691–707. https://doi.org/10.1364/OE.22.031691<http://www.opticsexpress.org/abstract.cfm?URI=oe-22-26-31691>.
[33] Mack CA. Generating random rough edges, surfaces, and volumes. Appl Opt 2013;52(7):1472–80. https://doi.org/10.1364/AO.52.001472<http://ao.osa.org/abstract.cfm?URI=ao-52-7-1472>.
[34] Yura HT, Hanson SG. Digital simulation of an arbitrary stationary stochastic process by spectral representation. J Opt Soc Am A 2011;28(4):675–85. https://doi.org/10.1364/JOSAA.28.000675<http://josaa.osa.org/abstract.cfm?URI=josaa-28-4-675>.
[35] Goldstein DH. Polarized light. 3rd ed. Boca Raton, FL: CRC; 2011.
[36] Goodman JW. Introduction to fourier optics. 3rd Edition Englewood, CO: Roberts & Company; 2005.
[37] Optics Meadowlark. Spatial light modulator—512 × 512. Data Sheet 2018.
[38] Voelz DG. Computational Fourier optics: a MATLAB tutorial. Bellingham, WA: SPIE Press; 2011.
[39] Schmidt JD. Numerical simulation of optical wave propagation with examples in MATLAB. Bellingham, WA: SPIE Press; 2010.